

Real-time imaging of laser-driven nanoplasma expansion

C. Peltz,¹ J.A. Powell,^{2,3,4} P. Rupp,⁵ A Summers,^{2,6} T. Gorkhover,^{7,8} M. Gallei,⁹ I. Halfpap,¹⁰ E. Antonsson,¹⁰ B. Langer,¹⁰ C. Trallero-Herrero,^{2,3} C. Graf,¹¹ D. Ray,⁷ Q. Liu,^{5,12} T. Osipov,⁷ M. Bucher,⁷ K. Ferguson,⁷ S. Möller,⁷ S. Zherebtsov,⁵ D. Rolles,² E. Rühl,¹⁰ G. Coslovich,⁷ R. N. Coffee,^{7,13} C. Bostedt,^{14,15,16} A. Rudenko,² M.F. Kling,^{5,12} and T. Fennel^{1,17}

¹*Institute for Physics, Universität Rostock, D-18051 Rostock, Germany*

²*J.R. Macdonald Laboratory, Department of Physics,
Kansas State University, Manhattan, Kansas 66506, USA*

³*Department of Physics, University of Connecticut, Storrs, Connecticut 06269, USA*

⁴*INRS, Énergie, Matériaux et Télécommunications,
1650 Blvd. Lionel Boulet, Varennes, Québec, J3X 1S2, Canada*

⁵*Department of Physics, Ludwig-Maximilians-Universität
Munich, D-85748 Garching, Germany*

⁶*ICFO - The Institute of Photonic Sciences,
The Barcelona Institute of Science and Technology,
08860 Castelldefels, Barcelona, Spain*

⁷*Linac Coherent Light Source, SLAC National
Accelerator Laboratory, Menlo Park, CA 94025, USA*

⁸*University of Hamburg, Institute for Experimental Physics, 22761 Hamburg, Germany*

⁹*Saarland University, D-66123 Saarbrücken, Germany*

¹⁰*Physical Chemistry, Freie Universität Berlin, D-14195 Berlin, Germany*

¹¹*Department of Chemistry and Biotechnology,
Darmstadt University of Applied Sciences, D-64295 Darmstadt, Germany*

¹²*Max Planck Institute of Quantum Optics, D-85748 Garching, Germany*

¹³*The Pulse Institute, SLAC National Accelerator Laboratory, Menlo Park, CA 94028, USA*

¹⁴*Chemical Sciences and Engineering Division,
Argonne National Laboratory, Argonne, Illinois 60439, USA*

¹⁵*Paul-Scherrer Institute, CH-5232 Villigen PSI, Switzerland*

¹⁶*LUXS Laboratory for Ultrafast X-ray Sciences,
Institute of Chemical Sciences and Engineering,*

École Polytechnique Fédérale de Lausanne (EPFL), CH-1015 Lausanne, Switzerland

¹⁷Max Born Institute, D-12489 Berlin, Germany

(Dated: September 22, 2021)

Abstract

The free expansion of a planar plasma surface is a fundamental non-equilibrium process relevant for various fields but as-yet experimentally still difficult to capture. The significance of the associated spatiotemporal plasma motion ranges from astrophysics and controlled fusion to laser machining, surface high-harmonic generation, plasma mirrors, and laser-particle acceleration. Here, we show that x-ray coherent diffractive imaging can surpass existing approaches and enables the quantitative real-time analysis of the sudden free expansion of nanoplasmas. For laser-ionized SiO₂ nanospheres, we resolve the formation of the emerging nearly self-similar plasma profile evolution and expose the so far inaccessible shell-wise expansion dynamics including the associated startup delay and rarefaction front velocity. Our results establish time-resolved diffractive imaging as an accurate quantitative diagnostic platform for tracing and characterizing plasma expansion and indicate the possibility to resolve various laser-driven processes including shock formation and wave-breaking phenomena with unprecedented resolution.

The sudden free expansion of a plasma with an initially sharp density step is a key model process for astrophysical flows [1], fusion pellet ablation [2, 3], and plasma dynamics initiated by discharges [4] or wire explosions [5, 6]. Especially the occurrence and structure of expansion modes with self-similar density evolution [7] has been subject of vivid debate and intense analytical and numerical analysis [8–11]. The significance of free plasma expansion culminates in the realm of intense laser-matter interactions at surfaces due to its central role for laser-driven monoenergetic ion beam generation [12, 13], vacuum acceleration of electrons [14], high-harmonic generation through relativistic oscillating mirrors [15–17] or coherent wake emission [18, 19], and pulse cleaning via transient plasma mirrors [20]. In all these cases, the plasma density profile at the surface is a pivotal element or critical control parameter for the main process. Moreover, access to the surface expansion speed of isochorically heated plasmas enables characterization of thermophysical properties of warm dense matter [21, 22], underlining the far-reaching implications of an accurate characterization and understanding of plasma profile and expansion velocity dynamics.

Established approaches for the experimental characterization of laser-induced plasma expansion include shadowgraphy and fluorescence imaging [21, 23], optical interferometry [24], Doppler spectroscopy [25], and proton imaging [26], each with its specific merits. However, for the complete characterization of the microscopic expansion process including the formation and evolution of self-similar expansion modes, simultaneous resolution of density and velocity profiles on nanometer spatial and femtosecond temporal scales or even beyond is essential, which exceeds current capabilities and is so far restricted to simulations.

An emerging alternative towards ultrafast and accurate tracing of plasma dynamics is time-resolved coherent diffractive imaging of laser-driven free nanoparticles using x-ray free electron lasers (XFEL) [27]. Complete atomistic pump-probe simulations of ultrafast near-infrared (NIR) laser-driven ionization and heating of hydrogen nanospheres have predicted the rapid formation of a nearly self-similar expansion mode for the initially step-like density profile [28]. The main short-term dynamics is predicted to unfold within few femtoseconds and includes an inward-motion of the rarefaction front due to a decreasing radius of the dense plasma core, an increasing softness of the density edge, and the spreading of the expanding surface layer (see Fig. 1i) that maintains a density profile with an asymptotically exponential radial decay. Most importantly, a direct mapping between x-ray scattering patterns and the associated plasma profile parameters has been identified for nearly spherical particles,

promising the experimental characterization of the density profile evolution with high spatial and temporal resolution.

In a pioneering study, Gorkhover *et al.* demonstrated a substantial expansion of the surface layer of laser-heated Xe clusters on the few hundred fs time scale [29] by analyzing the evolution of the angular decay of the ring-shaped diffraction fringes. Wide angle Bragg scattering with hard XFEL pulses can yield insights into the dynamics of strongly pumped nanoplasmas [30], indicating that the loss of order proceeds from the surface to the inner core of the cluster [31]. Diffraction experiments on laser-driven metal gratings further support high sensitivity of scattering patterns to the ultrafast density profile evolution at the surface [32]. However, the envisaged complete tracing of the laser-induced plasma expansion has so far remained a challenge as it requires the combination of (i) accurate knowledge of the target’s initial size and shape, (ii) an unambiguous profile reconstruction based on an appropriate few-parameter profile model, (iii) precise single-shot pulse timing to remedy the otherwise pathological time jitter of free-electron laser sources when operated in self-amplified spontaneous emission (SASE) mode, and (iv) a sufficiently large dataset to trace the profile evolution systematically.

Here, we report simultaneous realization of all the above prerequisites and demonstrate quantitative time-resolved imaging of laser-induced nanoplasma expansion. The NIR pump x-ray diffraction probe experiment was performed for isolated SiO₂ nanospheres at the Linac Coherent Light Source (LCLS) at SLAC and exposes the density profile evolution with unprecedented temporal and spatial resolution. Moreover, our analysis provides access to the so far inaccessible shell-resolved expansion startup delay and velocity buildup as well as the associated rarefaction front velocity. These results define not only a critical benchmark for theory but also enable the systematic study of the impact of laser characteristics and material properties on the ultrafast formation and relaxation of laser-driven nanoplasmas.

The measurement was performed at the AMO hutch of LCLS using the LAMP multi-purpose endstation, see schematic setup in Fig. 1(a). The beam of SiO₂ nanospheres with narrow distribution of size and deformation crossed the optical axis of the temporally synchronized and collinear NIR and x-ray pulses. For the employed NIR pulse parameters, strong and nearly homogeneous ionization of the resulting nanoplasma to atomic charge states $q \approx 6$ is expected [28, 33]. Single-shot x-ray scattering images are recorded with two rectangular pnCCD detector panels [34] that were covered by a spectral filter to suppress

NIR photons and XUV fluorescence from the heated nanoplasma. Employing a smaller x-ray spot size and selecting only bright diffraction images enables the exclusive analysis of particle scattering images from a region that was homogeneously pumped by the NIR laser. Downstream the optical axis, the accurate relative timing of the x-ray and NIR pulses is measured on a single shot basis with few-femtosecond accuracy (see Methods) [35–37].

Single-shot diffraction images were systematically recorded as function of pulse delay. While scattering patterns with bright, nearly spherical fringes from unpumped particles are observed for negative pulse delay (x-rays first), the fringe features begin to move and fade with increasing delay for pumped particles (positive delays), see Fig. 1(d-g). The evolution of the fringe pattern represents our main observable and encodes the plasma density dynamics. Note that images from unpumped particles enable the in-situ characterization of the initial target size distribution (see Fig. 1b).

From 1.3×10^6 recorded scattering images we found 24500 clearly identifiable hits. After removing faint images, multiparticle hits that display Newton rings [38, 39], and hits from clustered nanoparticles, a dataset of 5700 bright single-shot images with clear fringe structures has been systematically analyzed as described below. Out of that, a subset of 1070 images was assigned to the high intensity region of the x-ray focus which is associated with homogeneous NIR pumping. It should be emphasized that the latter discrimination step cannot be made based on the scattering pattern alone but requires the quantitative fit of the image with our model to determine the associated incident x-ray fluence (see Methods). The distributions of classified images versus pulse delay are displayed in Fig. 1c.

Individual scattering images are analyzed by fitting scattering patterns calculated for a simulation-guided few-parameter shape model [28] assuming an electron density profile described by a modified Fermi function with

$$n(\vec{r}) = \frac{n_0}{\left[\exp\left(\frac{\kappa(\vec{r})}{\lambda\sigma}\right) + 1 \right]^\sigma}. \quad (1)$$

Here n_0 is the core electron density, κ is the local surface offset of the sampling point \vec{r} , σ is the edge softness parameter, and λ is the scale length of the density decay. A sharp density edge corresponds to the limit $\sigma \rightarrow 0$. For a spherical reference surface with radius R , the surface offset is $\kappa = r - R$. Note, however, that the slight ellipsoidal deformation of the nanospheres resulting from the particle synthesis must be included for high accuracy fits (see Supplementary Information). For the resulting ellipsoidal reference surface with direction

dependent radius, the local surface offset is defined as $\kappa = [\vec{r} - \vec{\rho}] \cdot \vec{n}$, where $\vec{\rho}(\vec{r})$ specifies the closest point on the reference surface and \vec{n} is the associated unit vector of the surface normal. The neglect of directional variations of the remaining relevant parameters σ and λ is justified by the small anisotropy predicted by microscopic calculations [28]. For the fitting procedure we consider small-angle scattering within the first Born approximation such that the scattering image reflects the Fourier transform of the projected electron density (see Methods).

For a given value of the edge softness parameter σ , high quality fits of individual images can be performed and yield the scale length λ and the minimal and maximal core radii ρ_{\min} and ρ_{\max} that characterize the minor and major axis of the projected density associated with the ellipsoidal control surface (see Supplementary Information). For further analysis we use the effective radius $R_{\text{eff}} = \frac{\rho_{\min} + \rho_{\max}}{2}$. In the limit of vanishing softness (sharp edge), the spacing and angular decay of the diffraction fringes encode the core radius and scale length directly and almost independently. For finite edge softness, however, their values remain dependent on the value of the edge softness parameter, resulting in an apparent critical ambiguity for the analysis if the value or evolution of the softness parameter is unknown. In previous work, the problem was usually circumvented by assuming an unphysical sharp edge. Here we resolve this ambiguity by exploiting the conservation of the number of scattering electrons (i.e conservation of mass in the case of charge neutrality), as described in the following.

To motivate the approach, Fig. 2a,b displays fit results for the delay dependent evolution of scale length and effective radius when assuming a fixed very sharp edge ($\sigma = 0.1$). In this case, the associated total mass (number of electrons contributing to the scattering as given by the integral of the electron density) would increase by almost 90% during the first 200 fs of the expansion (Fig. 2c), which is obviously unphysical. The profile parameters retrieved assuming a very soft edge ($\sigma = 0.9$) differ substantially (Fig. 2d,e) and, in turn, would correspond to a mass decrease by more than 20% (Fig. 2f). The mass mismatch evolution map resulting from fits with systematically varied softness parameters is shown in false color representation in Fig. 2j, where the above discussed representative cases are indicated by horizontal lines (top and bottom). While the impact of the edge softness on the mismatch is little for unpumped particles as its effect vanishes in the limit of small scale length (sharp density step), the map shows that mass conservation during expansion requires a dynamical

change of the softness parameter, expressed by the *path of mass conservation* (white color) in Fig. 2j. The delay dependent softness associated with conserved total mass (black curve) defines the final and physically consistent evolution of all parameters and their mean values, i.e. softness, scale length and core radius, see Figs. 2g-j. Only these parameters have been used for further analysis and in Fig. 1.

The resulting time-dependent density map in Fig. 3a displays the retrieved mean density profile evolution and reflects the core depletion and ablation dynamics of the nanoplasma. Both the decreasing radius of the remaining high-density core as well as the increasing width of the surface layer can be clearly identified and tracked in time, see the evolution of density isolines. Note that the initial finite width of the density step in the experimental data for unpumped particles (negative delays) is attributed to surface roughness and deviations from an ellipsoidal shape. Minimizing the initial roughness and surface porosity via advanced target preparation techniques is expected to remedy this effect [40]. Most importantly, the continuous sampling of the mean density profile along the time axis further allows to track the expansion startup and velocity buildup for individual shells - an information that could not be accessed with existing plasma imaging techniques. To that end we analyze the evolution of the normalized radial density integral. The resulting mass fraction map (Fig. 3b) reflects the relative particle mass enclosed in a given radius as function of time. Contours of equal mass fraction (see lines), in turn, reflect the expansion of individual shells and define meaningful shell-specific trajectories if overrun effects (i.e. if inner shells overrun outer ones) can be excluded.

The evolution of adjacent shell trajectories shows that the surface layer expansion does not proceed with a single speed. From the shell-resolved trajectories we can extract the specific buildup and saturation of the respective shell velocities as well as the associated start-up delay. A comparison of the shell-specific start-up delays (symbols in Fig. 3b), however, shows an almost constant velocity of the inward-traveling rarefaction front with radial speed $v_{\text{front}}^{\text{exp}} = -0.135 \text{ nm/fs}$ and defines a global startup delay of $\tau_{\text{startup}}^{\text{exp}} = 52 \text{ fs}$ via interpolation to the initial surface radius (see Fig. 3b). These two central parameters, i.e. the front velocity and the global start-up delay, are assumed to be characteristic observables for the dependence of the plasma formation and relaxation dynamics on laser parameters and material properties and are thus of particular interest for comparison with theory.

With existing models, a full microscopic modelling of the expansion dynamics for the

experimental scenario is still out of reach. However, to evaluate the significance and generic character of the observed features, we perform a qualitative comparison with the published microscopic particle-in-cell simulations for hydrogen spheres [28], see Fig. 3c,d. The simulation results are displayed for axis limits that correspond to similar relative changes of parameters as in the experiment. Though absolute spatial and temporal scales are different, the general structure of the density evolution and shell-resolved expansion trajectories shows excellent agreement. In particular, a finite start-up delay of $\tau_{\text{startup}}^{\text{sim}} = 7$ fs and a nearly constant rarefaction front velocity of $v_{\text{front}}^{\text{exp}} = -0.035$ nm/fs are predicted by the simulations, supporting general applicability of our analysis and the significance of these key parameters. In particular, our results demonstrate the accessibility of these parameters in time-resolved diffraction studies, highlighting their potential for the quantitative characterization of both laser-driven plasma formation and the resulting relaxation in both experiment and theory. The development of theoretical models that can explain the impact of material and laser parameters is expected to allow the description and optimization of such processes for arbitrary target shapes and laser configurations.

Our time-resolved diffraction experiment has revealed the quantitative density profile evolution emerging in the early stage of sudden laser-induced nanoplasma expansion for silica nanospheres. The work exposes the so-far inaccessible onset, buildup, and stabilization of the shell-resolved expansion velocity. The observed rarefaction front velocity is comparable with the disorder front velocity reported in [31], indicating a potential connection between the two observables that remains to be clarified. The current results provide a critical reference for theory and underpin the unprecedented potential of diffractive imaging for the precise characterization of ultrafast laser-plasma processes, with far-reaching implications for both fundamental research on laser-induced self-similar plasma expansion and applications of intense laser-matter interactions at plasma surfaces in general. The feasibility of ultrafast imaging with simultaneous high spatial and temporal resolution is expected to also enable tracking of other ultrafast plasma dynamics, such as bunching and shock formation in the expansion process [9] or nonlinear plasma wave formation and breaking [33]. Our method is further anticipated to be transferable to thin cylindrical or even flat jets, opening routes to the systematic tracking of plasma formation, wave dynamics, and the initial phases of ablation in various materials including biologically relevant liquids such as liquid water.

Acknowledgements

Use of the Linac Coherent Light Source (LCLS), SLAC National Accelerator Laboratory, is supported by the U.S. Department of Energy, Office of Science, Office of Basic Energy Sciences under Contract No. DE-AC02-76SF00515. RNC and GC are funded through the LCLS under contract number DE-AC02-76SF00515. This material is based on work supported by the U.S. Department of Energy, Office of Basic Energy Sciences, Division of Chemical Sciences, Geosciences, and Biosciences through Argonne National Laboratory under contract DE-AC02-06CH11357. A.R. and D.R. were supported by the US Department of Energy, Office of Science, Office of Basic Energy Sciences, Division of Chemical, Geological and Biological Sciences (contract no. DE-FG02-86ER13491). J.A.P and C.T.-H. acknowledge support from the Air Force Office of Scientific Research (contract no. FA9550-17-1-0369). We thank Al Rankin for his help in preparing the nanoparticle injector for this experiment and Julia Kredel for support in the particle synthesis. T.F. acknowledges financial support from the Deutsche Forschungsgemeinschaft (DFG) via SFB 652/3 (ID: 5486320), within the Heisenberg programme (IDs: 315210756, 398382624, 436382461), and via DFG Priority Programme QUTIF (ID: 281272685). Computer time was provided by the North-German Supercomputing Alliance (HLRN) via project mvp00013. M.F.K. acknowledges support from the Max Planck Society via the Max Planck Fellow program, and the DFG via the Priority Programme QUTIF (ID: 281272685). S.Z. acknowledges support from the DFG via project no. 322422731. C.B. acknowledges support via the Swiss National Science Foundation National Center of Competence in Research – Molecular Ultrafast Science and Technology NCCR - MUST.

Author contributions

C.P., C.B., A.R., M.F.K., and T.F. conceived the experiment. M.G., E.R. and C.G. prepared the targets and performed the TEM analysis. J.A.P, P.R, A.S., C.T.-H., M.F.K. and A.R. designed and build the nanoparticle injector. C.P., J.A.P., P.R., A.S., T.G., I.H., E.A., B.L., D.R., Q.L., T.O., M.B., K.F., S.M., D.R., E.R., G.C., R.N.C., C.B. and M.F.K. performed the experiment. C.P. and T.F. wrote the manuscript, with input from all co-

authors.

-
- [1] J. Borovsky, M. Pongratz, R. Rousseldupre, and T. Tan, *Astrophys. J.* **280**, 802 (1984), URL <https://doi.org/10.1086/162054>.
- [2] C. Chang, L. Jorgensen, P. Nielsen, and L. Lengye, *Nucl. Fusion* **20**, 859 (1980), URL <https://doi.org/10.1088/0029-5515/20/7/008>.
- [3] S. Milora, W. Houlberg, L. Lengyel, and V. Mertens, *Nucl. Fusion* **35**, 657 (1995), URL <https://doi.org/10.1088/0029-5515/35/6/I04>.
- [4] R. Tanberg, *Phys. Rev.* **35**, 1080 (1930), URL <https://doi.org/10.1103/PhysRev.35.1080>.
- [5] B. Eiselt, *Z. Phys.* **132**, 54 (1952), URL <https://doi.org/10.1007/BF01338576>.
- [6] C. Nash and W. Mcmillan, *Phys. Fluids* **4**, 911 (1961), URL <https://doi.org/10.1063/1.1706424>.
- [7] A. V. Gurevich, L. Pariiska, and L. Pitaevskii, *Sov. Phys. JETP* **22**, 449 (1966).
- [8] M. True, J. Albritton, and E. Williams, *Phys. Fluids* **24**, 1885 (1981), URL <https://doi.org/10.1063/1.863270>.
- [9] C. Sack and H. Schamel, *Phys. Rep.* **156**, 311 (1987), URL [https://doi.org/10.1016/0370-1573\(87\)90039-1](https://doi.org/10.1016/0370-1573(87)90039-1).
- [10] M. Murakami and M. Basko, *Phys. Plasmas* **13** (2006), URL <https://doi.org/10.1063/1.2162527>.
- [11] A. Beck and F. Pantellini, *Plasma Phys. Control. Fusion* **51** (2009), URL <https://doi.org/10.1088/0741-3335/51/1/015004>.
- [12] P. Mora, *Phys. Rev. Lett.* **90**, 185002 (2003), URL <https://doi.org/10.1103/PhysRevLett.90.185002>.
- [13] H. Daido, M. Nishiuchi, and A. S. Pirozhkov, *Rep. Prog. Phys.* **75**, 056401 (2012), URL <https://doi.org/10.1088/0034-4885/75/5/056401>.
- [14] M. Thevenet, A. Leblanc, S. Kahaly, H. Vincenti, A. Vernier, F. Quere, and J. Faure, *Nat. Phys.* **12**, 355 (2016), URL <https://doi.org/10.1038/NPHYS3597>.
- [15] S. Bulanov, N. Naumova, and F. Pegoraro, *Phys. Plasmas* **1**, 745 (1994), URL <https://doi.org/10.1063/1.870766>.
- [16] G. A. Mourou, T. Tajima, and S. V. Bulanov, *Rev. Mod. Phys.* **78**, 309 (2006), URL <https://doi.org/10.1063/1.2228000>.

- [//doi.org/10.1103/RevModPhys.78.309](https://doi.org/10.1103/RevModPhys.78.309).
- [17] C. Roedel, D. an der Bruegge, J. Bierbach, M. Yeung, T. Hahn, B. Dromey, S. Herzer, S. Fuchs, A. G. Pour, E. Eckner, et al., *Phys. Rev. Lett.* **109**, 125001 (2012), URL <https://doi.org/10.1103/PhysRevLett.109.125002>.
- [18] F. Quere, C. Thaury, P. Monot, S. Dobosz, P. Martin, J. Geindre, and P. Audebert, *Phys. Rev. Lett.* **96** (2006), URL <https://doi.org/10.1103/PhysRevLett.96.125004>.
- [19] A. Borot, A. Malvache, X. Chen, A. Jullien, J.-P. Geindre, P. Audebert, G. Mourou, F. Quere, and R. Lopez-Martens, *Nat. Phys.* **8**, 416 (2012), URL <https://doi.org/10.1038/NPHYS2269>.
- [20] C. Thaury, F. Quere, J.-P. Geindre, A. Levy, T. Ceccotti, P. Monot, M. Bougeard, F. Reau, P. D'Oliveira, P. Audebert, et al., *Nat. Phys.* **3**, 424 (2007), URL <https://doi.org/10.1038/nphys595>.
- [21] W. Bang, B. J. Albright, P. A. Bradley, D. C. Gautier, S. Palaniyappan, E. L. Vold, M. A. S. Cordoba, C. E. Hamilton, and J. C. Fernandez, *Sci. Rep.* **5**, 14318 (2015), URL <https://doi.org/10.1038/srep14318>.
- [22] W. Bang, B. J. Albright, P. A. Bradley, E. L. Vold, J. C. Boettger, and J. C. Fernandez, *Sci. Rep.* **6**, 29441 (2016), URL <https://doi.org/10.1038/srep29441>.
- [23] S. S. Harilal, P. J. Skrodzki, A. Miloshevsky, B. E. Brumfield, M. C. Phillips, and G. Miloshevsky, *Phys. Plasmas* **24**, 063304 (2017), URL <https://doi.org/10.1063/1.4985678>.
- [24] J. Wang, F. Coppari, R. F. Smith, J. H. Eggert, A. E. Lazicki, D. E. Fratanduono, J. R. Rygg, T. R. Boehly, G. W. Collins, and T. S. Duffy, *Phys. Rev. B* **92**, 174114 (2015), URL <https://doi.org/10.1103/PhysRevB.92.174114>.
- [25] S. Mondal, A. D. Lad, S. Ahmed, V. Narayanan, J. Pasley, P. P. Rajeev, A. P. L. Robinson, and G. R. Kumar, *Phys. Rev. Lett.* **105**, 105002 (2010), URL <https://doi.org/10.1103/PhysRevLett.105.105002>.
- [26] L. Romagnani, J. Fuchs, M. Borghesi, P. Antici, P. Audebert, F. Ceccherini, T. Cowan, T. Grismayer, S. Kar, A. Macchi, et al., *Phys. Rev. Lett.* **95**, 195001 (2005), URL <https://doi.org/10.1103/PhysRevLett.95.195001>.
- [27] H. N. Chapman, S. P. Hau-Riege, M. J. Bogan, S. Bajt, A. Barty, S. Boutet, S. Marchesini, M. Frank, B. W. Woods, W. H. Benner, et al., *Nature* **448**, 676 (2007), URL <https://doi.org/10.1038/nature06049>.

- [28] C. Peltz, C. Varin, T. Brabec, and T. Fennel, *Phys. Rev. Lett.* **113**, 133401 (2014), URL <https://doi.org/10.1103/PhysRevLett.113.133401>.
- [29] T. Gorkhover, S. Schorb, R. Coffee, M. Adolph, L. Foucar, D. Rupp, A. Aquila, J. D. Bozek, S. W. Epp, B. Erk, et al., *Nat. Photon.* **10**, 93 (2016), URL <https://doi.org/10.1038/NPHOTON.2015.264>.
- [30] K. R. Ferguson, M. Bucher, T. Gorkhover, S. Boutet, H. Fukuzawa, J. E. Koglin, Y. Kumagai, A. Lutman, A. Marinelli, M. Messerschmidt, et al., *Sci. Adv.* **2**, e1500837 (2016), URL <https://doi.org/10.1126/sciadv.1500837>.
- [31] T. Nishiyama, Y. Kumagai, A. Niozu, H. Fukuzawa, K. Motomura, M. Bucher, Y. Ito, T. Takanashi, K. Asa, Y. Sato, et al., *Phys. Rev. Lett.* **123**, 123201 (2019), URL <https://doi.org/10.1103/PhysRevLett.123.123201>.
- [32] T. Kluge, M. Roedel, J. Metzkes-Ng, A. Pelka, A. L. Garcia, I. Prencipe, M. Rehwald, M. Nakatsutsumi, E. E. McBride, T. Schoenherr, et al., *Phys. Rev. X* **8**, 031068 (2018), URL <https://doi.org/10.1103/PhysRevX.8.031068>.
- [33] C. Varin, C. Peltz, T. Brabec, and T. Fennel, *Phys. Rev. Lett.* **108**, 175007 (2012), URL <https://doi.org/10.1103/PhysRevLett.108.175007>.
- [34] L. Strüder, S. Eppa, D. Rolles, R. Hartmann, P. Holl, G. Lutz, H. Soltau, R. Eckart, C. Reich, K. Heinzinger, et al., *Nuclear Instrum. Methods A* **614**, 483 (2010), URL <https://doi.org/10.1016/j.nima.2009.12.053>.
- [35] S. Schorb, T. Gorkhover, J. P. Cryan, J. M. Glowia, M. R. Bionta, R. N. Coffee, B. Erk, R. Boll, C. Schmidt, D. Rolles, et al., *Applied Physics Letters* **100**, 121107 (2012), URL <https://doi.org/10.1063/1.3695163>.
- [36] M. Beye, O. Krupin, G. Hays, A. H. Reid, D. Rupp, S. d. Jong, S. Lee, W.-S. Lee, Y.-D. Chuang, R. Coffee, et al., *Appl. Phys. Lett.* **100**, 121108 (2012), URL <https://doi.org/10.1063/1.3695164>.
- [37] M. Harmand, R. Coffee, M. R. Bionta, M. Chollet, D. French, D. M. Fritz, H. Lemke, N. Medvedev, B. Ziaja, S. Toleikis, et al., *Nat. Photon.* **7**, 215 (2013), URL <https://doi.org/10.1038/nphoton.2013.11>.
- [38] C. Bostedt, M. Adolph, E. Eremina, M. Hoener, D. Rupp, S. Schorb, H. Thomas, A. R. B. de Castro, and T. Moeller, *J. Phys. B: At. Mol. Opt. Phys.* **43** (2010), URL <https://doi.org/10.1088/0953-4075/43/19/194011>.

- [39] D. Rupp, M. Adolph, T. Gorkhover, S. Schorb, D. Wolter, R. Hartmann, N. Kimmel, C. Reich, T. Feigl, A. R. B. de Castro, et al., *New. J. Phys.* **14** (2012), URL <https://doi.org/10.1088/1367-2630/14/5/055016>.
- [40] C. Raschpichler, C. Goroncy, B. Langer, E. Antonsson, B. Wassermann, C. Graf, P. Klack, T. Lischke, and E. Rühl, *J. Phys. Chem. C* **124**, 16663 (2020), URL <https://doi.org/10.1021/acs.jpcc.0c04308>.
- [41] W. Stöber, A. Fink, and E. Bohn, *J. Colloid Interf. Sci.* **26**, 62 (1968), URL [https://doi.org/10.1016/0021-9797\(68\)90272-5](https://doi.org/10.1016/0021-9797(68)90272-5).
- [42] C. Graf and A. van Blaaderen, *Langmuir* **18**, 524 (2002), URL <https://doi.org/10.1021/1a011093g>.
- [43] K. R. Ferguson, M. Bucher, J. D. Bozek, S. Carron, J.-C. Castagna, R. Coffee, G. I. Curiel, M. Holmes, J. Krzywinski, M. Messerschmidt, et al., *J. Synchrot. Radiat.* **22**, 492 (2015), URL <https://doi.org/10.1107/S1600577515004646>.
- [44] M. R. Bionta, H. T. Lemke, J. P. Cryan, J. M. Glownia, C. Bostedt, M. Cammarata, J.-C. Castagna, Y. Ding, D. M. Fritz, A. R. Fry, et al., *Opt. Express* **19**, 21855 (2011), URL <https://doi.org/10.1364/OE.19.021855>.
- [45] M. R. Bionta, N. Hartmann, M. Weaver, D. French, D. J. Nicholson, J. P. Cryan, J. M. Glownia, K. Baker, C. Bostedt, M. Chollet, et al., *Rev. Sci. Instrum.* **85**, 083116 (2014), URL <https://doi.org/10.1063/1.4893657>.
- [46] J. M. Glownia, J. Cryan, J. Andreasson, A. Belkacem, N. Berrah, C. I. Blaga, C. Bostedt, J. Bozek, L. F. DiMauro, L. Fang, et al., *Opt. Express* **18**, 17620 (2010), URL <https://doi.org/10.1364/OE.18.017620>.
- [47] R. N. Coffee, L. Fang, and G. N. Gibson, *Phys. Rev. A* **73**, 043417 (2006), URL <https://doi.org/10.1103/PhysRevA.73.043417>.

Methods

A. Target preparation and characterization

Silica nanoparticles were produced by the Stöber method [41]. First, small seed nanoparticles were prepared by adding 21 g of TEOS, 28 mL of ammonia solution (25%wt. in water)

and 1 mL of water to 530 mL of ethanol and stirring the mixture for 24 h. A further shell was grown on the seed nanoparticles via the seeded growth method [42] until the desired particle size was reached. All samples were stored in ultra-pure ethanol after cleaning. The used particle batch was characterized by means of transmission electron microscopy (TEM) as well as by fits of the scattering pattern from unpumped particles (cf. Fig. 1a). The TEM analysis yields an average diameter of 125.2 nm and a polydispersity of 1.8% while a mean diameter of 123.5 nm and a polydispersity of 2.3% is determined from the scattering pattern. Note that these values are consistent when considering the estimated systematic error of ca. 2% in the analysis of the diffraction data due to uncertainty of the exact distance of the active detector plane from the interaction point and the fluctuation of the central X-ray wavelength. Suitable aliquots of the mother suspension were dispersed in larger volumes in deionized water at a concentration of 1 g/l, then briefly sonicated, and used in the experiments. The nanoparticles are aerosolized with nitrogen. The aerosol was subsequently dried in a counterflow membrane dryer employing dry nitrogen, introduced into the vacuum chamber through a 120 μm glass nozzle, and collimated by a differentially pumped aerodynamic lens to form a beam of nanoparticles.

B. Scattering detector and spectral filters

Scattering images are recorded in single-shot mode using the front pixel detectors of the LAMP endstation at LCLS [34, 43]. The front pixel detector consists of two movable detector panels, each containing 1024x512 pixel with 75x75 μm pixel size. The detectors are covered with a 50nm Al coating to suppress signal from visible light and plasma emission from the target into the extreme ultraviolet spectral regime. For the current experiments with intense 800nm laser pulses, an additional optical filter of 220nm Al on a 0.77 μm LUXfilm polyimide is used and a baffle system is implemented to guide the optical laser pulses through the detector system. The spectral transmission of the filter combined with the detector response [34] result in a net quantum efficiency of 0.48 for detection of the 800 eV XFEL photons employed for the diffractive imaging with single photon sensitivity.

C. Laser pulse characterization and timing analysis

Our results rely on the accurate determination of the relative delay between the NIR pump pulses and the x-ray scattering probe pulses. The Self Amplification of Spontaneous Emission (SASE) process for Free Electron Lasers as used here produces X-ray pulse shapes whose average temporal shape is well behaved but the individual shots are a near stochastic collection of longitudinal optical modes. When we speak of the “duration” of the x-ray pulse, we are therefore speaking of the average duration that is typically a majority fraction of the electron bunch length used to produce the FEL pulse. In our case the electron bunch was measured to correspond to a duration of about 40–50 fs, where the average x-ray pulse duration would be expected in the vicinity of 30–40 femtoseconds FWHM, though we note that the average intensity distribution is not necessarily Gaussian in shape. The NIR pump pulse used in this experiment has been repeatedly measured consistent with 50 fs duration FWHM at the interaction point. We used the conventional method of optimizing this duration *in situ* by optimizing the ratio of high/low charge states of the strong field ionization of Argon and N_2 .

The NIR pump laser and the FEL are independent sources, and as such their relative timing can only be controlled at the accuracy level of the radio-frequency synchronization system. At the LCLS, this synchronization is typically on the order of a 150 fs rms and must be corrected by the use of a single-shot x-ray optical cross correlation method [35, 36]. The cross correlation method used here is based on the idea of encoding time onto the spectrum of an optical reference [44, 45]. This so-called “spectral encoding” allows for relative measurements with precision below 10 fs [37].

In order to identify the absolute time overlap between the NIR and the x-ray pulse, we used the method described in [46] whereby the photo-dissociation of quasi-bound N_2^{++} dications into N^+ fragment ions [47] serves as an indication of the x-ray induced appearance of N_2^{++} via the x-ray core ionization and subsequent normal Auger decay. If the NIR pulse arrives before the x-ray pulse, incapable of double photoionization, the results are the usual x-ray induced quasi-bound N_2^{++} . As the NIR pulse is scanned to later delays, a step-like feature due to NIR induced dissociation of quasi-bound N_2^{++} appears when plotting the ratio of N^+/N_2^{++} and this step indicates the absolute time overlap of the NIR and x-ray pulse. Comparing the width of the step, after sorting the shots based on the spectral encoding

signal, we find a step width that is consistent with sub-10 fs precision of the relative timing measurement, 50 fs FWHM duration of the NIR pulse, and $\lesssim 40$ fs duration of the average x-ray pulse. Details and corresponding figures are given in the Supplementary Information.

D. Reconstruction of scattering images

In the description of the scattering process, both plasma electrons as well as atomically bound electrons with binding energies smaller than the X-ray photon energy can be treated as free electrons. In contrast, the scattering contribution of strongly bound electrons is negligible, such as in the case of the silicon K-shell electrons in our scenario. It should further be noted, that the K-shell electrons of Si are effectively unreachable for the NIR-driven ionization. Hence the Si K-shell can be neglected for both ionization and the scattering process. As a result and assuming that the fraction of emitted electrons is negligible for the large particles considered here, the density of actively scattering electrons is representative for the atomic density and their number can be assumed to be constant.

The particle density profile is reconstructed from the measured scattering images by fitting simulated scattering images based on the simulation-guided, analytical few-parameter representation of the plasma density from Eq. (1) to the measured data. In this process the ellipsoidal deformation of the particles as well as background noise from the detectors is included. Details of the fitting procedure and examples are given in the Supplementary Information. The treatment of the scattering problem via the few-parameter profile enables systematic forward fitting of a large dataset with thousands of scattering images, including the determination of the relative incidence X-ray fluence. The latter information is pivotal for the discrimination of intense shots that are associated with homogeneous NIR pump intensity. It should be noted that resolution of the expected weak polarization induced radius asymmetry reported in [28] due to stronger heating of the particle poles would in principle be possible with our approach, but cannot be achieved in the current study due to too large initial spread of the particle deformation combined with lacking scattering signals in the slit between the detector panels.

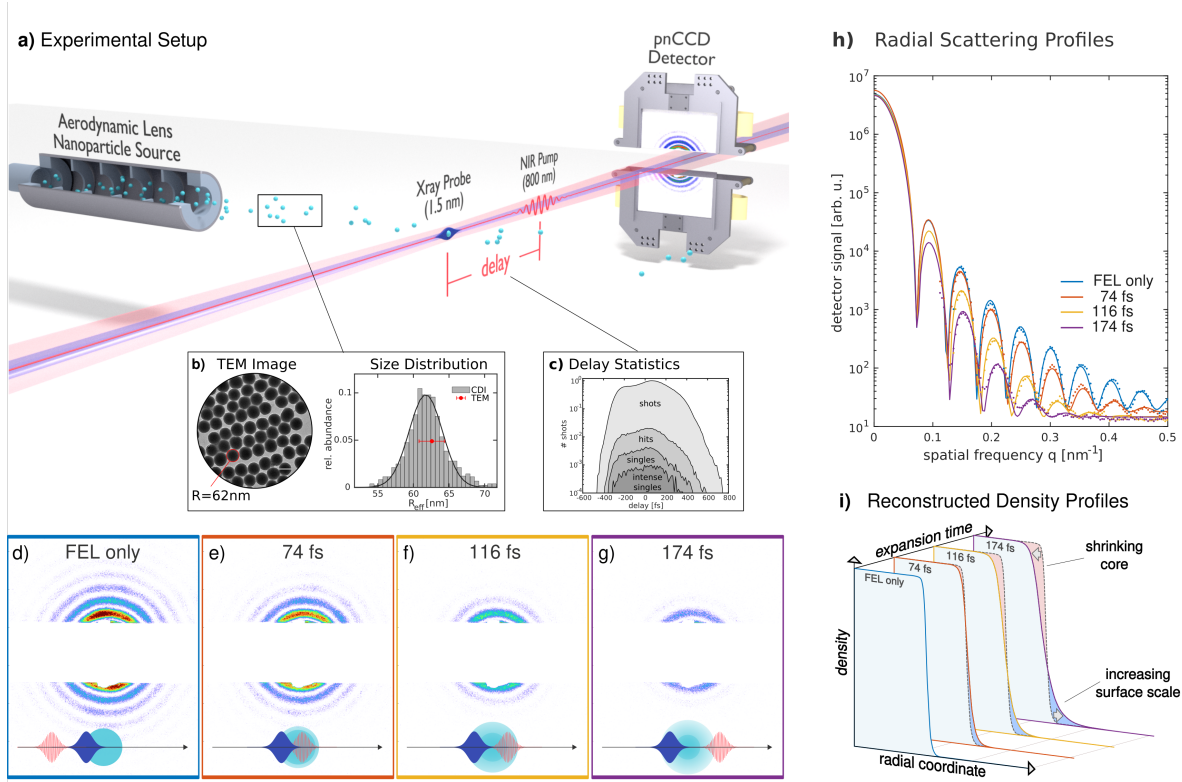


FIG. 1: **Sketch of the experiment.** (a) A beam of chemically prepared SiO_2 nanospheres with 62 nm mean radius was delivered into the interaction region by an aerosol source employing aerodynamic lens focusing. The width of the size distribution is characterized using both TEM images and the x-ray scattering pattern [see panel (b) and Methods]. X-ray pulses with 800 eV photon energy, 40 fs duration, and 1 mJ pulse energy are delivered at 120 Hz repetition rate and were focussed into the interaction region using a Kirkpatrick–Baez mirror system. They are merged with synchronized 50 fs NIR laser pulses at 800 nm central wavelength and intensity $8 \times 10^{14} \text{cm}^{-2}$ using a holey mirror placed behind the x-ray focusing optics. Scattering images are recorded by two pnCCD detector panels placed 40 cm behind the interaction zone. The gap between the detector panels transmits the primary beams of the x-ray and NIR lasers. Scattering images recorded for each laser shot are classified as hits, singles, and intense singles [see histograms in (c)] and only the latter are used for further analysis. The delay dependent scattering images are fitted with a model (see (d-g) for representative measured patterns and (h) for lineouts and associated fit results). (i) The associated reconstructed density profiles are displayed as function of the effective radial coordinate $r_{\text{eff}} = \kappa + R_{\text{eff}}$ (see text) and encode the plasma expansion. The profile dynamics resembles the laser-induced core shrinking and surface layer expansion (as indicated).

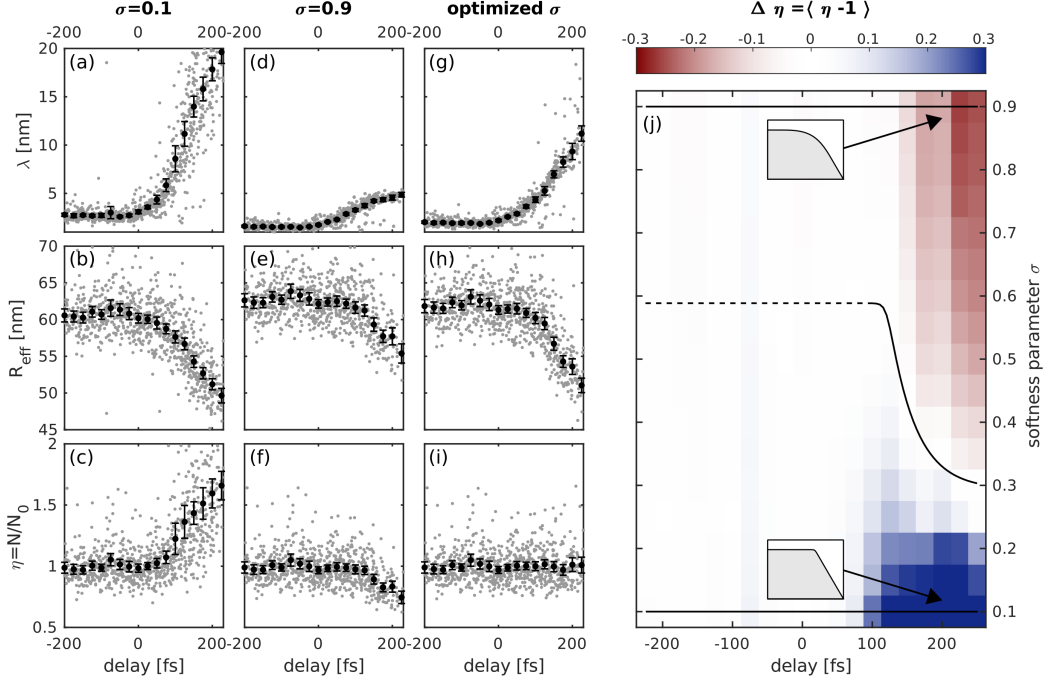


FIG. 2: **Reconstruction of the density profile parameters.** (a-i) Temporal evolution of surface width λ , effective core radius R_{eff} and associated relative mass $\eta = N/N_0$ reflecting the particle number $N = \int n(\vec{r})d^3r$ (\propto total mass) normalized to the average value for unpumped shots N_0 . Evolutions are displayed assuming a small (a-c), large (d-f), and the optimized softness parameter (g-i). Each gray dot represents an individual scattering image while the black symbols indicate the time-binned mean values and their corresponding standard deviations. A fixed sharp edge ($\sigma = 0.1$) leads to a strong overestimation of the particle number at large delays by roughly 70% (a-c). A fixed soft edge $\sigma = 0.9$ leads to the opposite effect, i.e. an unphysical mass loss with delay (d-f). A systematic analysis of the mass mismatch evolution versus softness yields a unique optimal path in the delay-softness plane that reflects mass conservation (j). Using $\sigma(t)$ determined by this optimal path leads to the final and physically consistent parameter evolution (g-j).

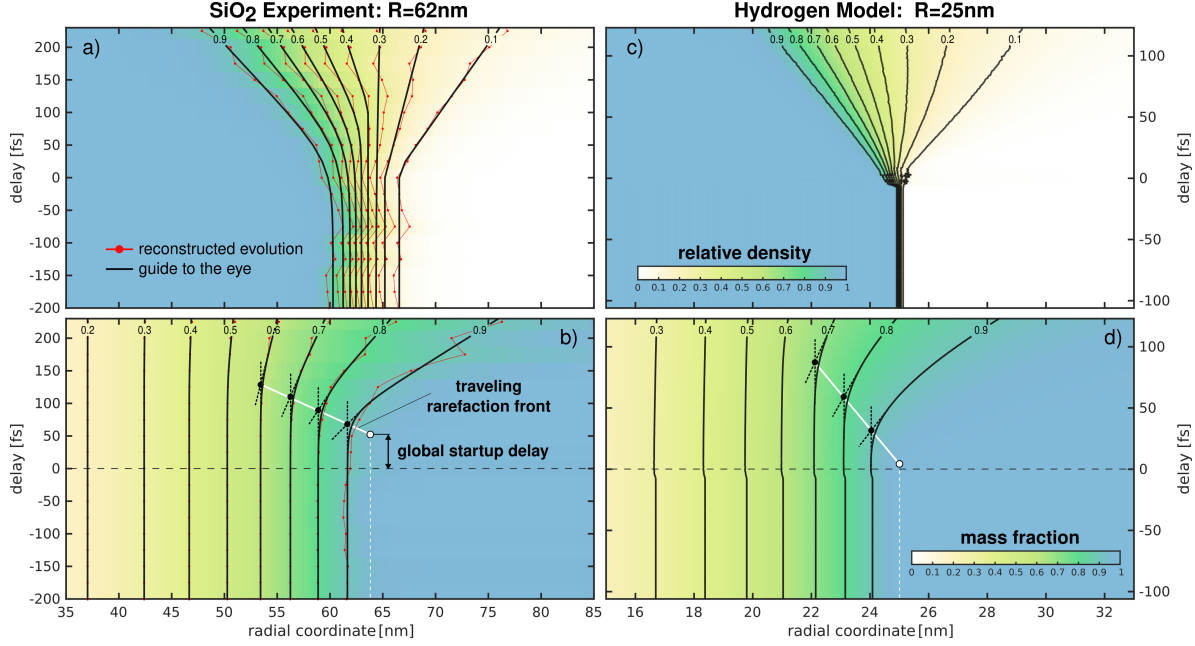


FIG. 3: **Evolution of radial density and mass fraction profiles.** (a,b) Reconstructed spatio-temporal density map and corresponding mass fraction map (color coded) with selected contour levels (red, levels as indicated) together with fit curves (solid) as guides to the eye. For qualitative comparison of the experimental features with available plasma model calculations, panels (c,d) show density and mass fraction maps (contour levels as indicated) as extracted from simulation results for hydrogen spheres [28]. Shell-specific expansion start-up times (black dots) in (b,d) are estimated as the intersection of the tangent to the trajectory at 2.5% relative shell expansion with the initial shell radius (c.f. black dotted lines). The global start-up delay (circle) is determined from extrapolation to the initial surface (see text), which we define as the radius where the initial relative density profile has dropped to $1/e$ (white dotted line). White solid lines indicate the motion of the rarefaction front.